High-content assay for precision medicine discovery in cystic fibrosis.

Stella Prins[1], Emily Langron[1], Cato Hastings[2], Emily Hill[1], Andra C. Stefan[3], Lewis D. Griffin[2] and Paola Vergani[1]*

[1] Department of Neuroscience, Physiology and Pharmacology

[2] CoMPLEX

[3] Natural Sciences

University College London

Gower Street

WC1E 6BT London UK

The first two authors contributed equally to this project.

*Correspondence to: p.vergani@ucl.ac.uk

Abstract

Cystic fibrosis (CF) is a life-limiting disease caused by mutations in the CFTR gene, which encodes an anion-selective channel. Because CF-causing mutations can affect CFTR gating as well as its biogenesis, multi-assay approaches have been implemented to sequentially screen for channel function and membrane density. Here we present the first assay capable of simultaneous assessment of both CFTR characteristics.

To validate our assay, we investigate F508del-CFTR, the most common disease-causing CFTR mutant, confirming rescue by incubation at low temperature, treatment with corrector VX-809 and introduction of the second-site revertant mutation R1070W. Furthermore, we confirm a decrease in F508del-CFTR membrane density due to presence of potentiator VX-770 during VX-809 treatment. Finally, we characterize a panel of rare CF-causing mutations, confirming profiles obtained with Western blots and Ussing-chamber electrophysiology. We discuss how profiling effects of acute VX-770 treatment on the rare mutation panel can provide mechanistic insight on drug action.

Because our assay quantifies simultaneously CFTR localization and function, it yields more accurate information on gating and permeation properties than can be inferred from separate measurements. By providing a two-dimensional molecular characterization of individual mutant CFTR proteins, our assay is a powerful tool for development of therapies truly addressing the root cause of each individual patient's cystic fibrosis disease.

Introduction

Cystic fibrosis (CF) is a life-limiting genetic disease most prevalent in people with a Caucasian background. Although the median survival age has increased by almost 12 years over the last decade, still only 50 percent of the people with CF are expected to live to 48 years of age (Cystic Fibrosis Trust UK, 2016), and the disease strongly impacts quality of life [1].

CF is caused by mutations in the *CFTR* gene [2, 3], encoding an anion-selective channel [4] present on the apical plasma membrane of epithelial cells. These mutations decrease the density of CFTR channels located on the cell membrane (by affecting protein synthesis, folding, intracellular trafficking, plasma membrane stability), and/or impair channel function (impacting on gating or anion permeation). As a result, transepithelial fluid movement is abnormal, creating a range of problems particularly affecting lungs, pancreas, intestines, liver and reproductive systems.

Electrophysiological methods are commonly used to describe CFTR channel properties: gating, quantified by open probability, P_O, and permeation, characterized by single-channel conductance, γ. Biogenesis and stability at the membrane are often monitored using biochemistry, especially protein immunoblots comparing complex-glycosylated (mature) to core-glycosylated (immature) CFTR. However, these techniques are not easily adapted to screening for drug development. Engineering of a halide sensitive YFP with increased affinity for iodide and a low affinity for chloride [5, 6], allowed the first high throughput screening projects, which assessed CFTR activity by measuring the rate of YFP quenching caused by iodide influx [7-10]. Later, changes in membrane potential monitored through fluorescence resonance energy transfer have been used by Vertex Pharmaceuticals to indirectly quantify CFTR channel function, allowing high-throughput screening of hundreds of thousands of compounds [11, 12].

This effort led to the identification of the first CFTR modulator drugs, directly targeting the defective CFTR protein and thus addressing the root cause of CF disease. These drugs have been classified as either “potentiators”, increasing CFTR channel function, or “correctors” boosting the number of CFTR channels on the plasma membrane. The potentiator ivacaftor (VX-770) [11] is now approved for the treatment of patients carrying the G551D gating mutation and a number of other mutations resulting in defective ion channel function (approximating 5% of the CF population [13]). However, neither potentiation of channel function by VX-770 on its own [14], nor treatment with the CFTR corrector VX-809 [15] alone [16], significantly improves lung function of patients homozygous for the F508del mutation,

present on at least one allele in ~90% of patients. Like many other CF-causing mutations, F508del results not only in ion channel dysfunction, but also in a reduction of the number of channels present at the cell surface. Unlike monotherapy, combination treatment with VX-770 and VX-809 provides small but significant health benefits [17]. Triple combination therapies, combining two different correctors with a potentiator, hold promise to further improve patient outcomes (e.g. [18, 19]).

Beside F508del, more than 300 CF-causing mutations have been characterized (The Clinical and Functional TRanslation of CFTR (CFTR2); available at http://cftr2.org). Each mutation, other than F508del, is extremely rare, making recruitment for clinical trials particularly difficult. In addition, each mutation is likely to affect the folding, trafficking, stability, gating dynamics and/or permeation of the encoded CFTR protein differently. With several CFTR-targeting compounds in the pipeline, high-quality pre-clinical data, informing on how drugs/drug combinations affect individual CFTR variants in simplified *in vitro* systems, is extremely valuable for drug development and trial design [20].

Here we present a medium-throughput image-based assay that acquires multi-dimensional data (dual-colour fluorescence intensity in time and space) on individual live HEK293 cells and extracts information on two key characteristics of CFTR. By co-expressing soluble mCherry with a halide sensitive YFP [5] linked to CFTR [21], our new assay gives readouts of both CFTR function, and CFTR membrane density. Experimental manipulation - incubation at low temperature [22-24], treatment with VX-809 [25, 26] with and without VX-770 [27, 28], and addition of revertant mutation R1070W [26, 29, 30] - results in the expected changes in measured F508del-CFTR channel function and membrane density. Furthermore, we present a screening platform suitable for profiling changes in the molecular characteristics of 62 CFTR variants carried by CF patients. Profiling of VX-770 (Vertex Pharmaceuticals) validates our new assay as a powerful tool for “high-content” CFTR monitoring in pharmacological research.

Results

The assay

To obtain quantitative information about ion channel function of CFTR, we exploited a halide-sensitive YFP (H148Q/I152L, [5, 6]), tagged to the N-terminal of CFTR [21, 31]. We constructed a pIRES2-mCherry-YFPCFTR plasmid that directs co-expression of

YFP(H148Q/I152L)-CFTR (hereafter designated YFP-WT-CFTR or simply WT-CFTR) and a soluble, cytosolic, red fluorescent protein, mCherry [32] (Figure 1a). The mCherry expression allows image segmentation and localization of the cell membrane by marking the border of cells. Furthermore, mCherry serves as an internal standard for the normalisation of YFP-CFTR expression, eliminating variability due to unequal transfection efficiency.

Yellow fluorescence at the boundaries of areas of red fluorescence, is used to estimate CFTR on the membrane (Figure 1). The "membrane" is defined as comprising a ~1 μm wide band, on the inside of a cell's boundary. In the representative cell transfected with YFP-F508del-CFTR, the F_{YFP} in the membrane zone is very similar to F_{YFP} outside the cell. However, in the cell transfected with YFP-WT-CFTR, there is a F_{YFP} peak in the membrane zone. The density of CFTR at the membrane (ρ), is estimated by dividing the average YFP-CFTR fluorescence intensity within the membrane zone ($F_{\mathrm{YFP\ membrane}}$), by the average mCherry fluorescence over the entire cell ($F_{\mathrm{mCherry\ cell}}$). The ρ metric can be thought of as the product of the proportion of CFTR localized to the membrane ($F_{\mathrm{YFP\ membrane}}/F_{\mathrm{YFP\ cell}}$), multiplied by the metabolic stability of YFP-CFTR with respect to mCherry ($F_{\mathrm{YFP\ cell}}/F_{\mathrm{mCherry\ cell}}$). Thus, changes in ρ metric will reflect not only changes in trafficking, but also changes in the overall rates of biosynthesis vs. degradation of the protein.

Increasing F508del-CFTR membrane density

To validate our new assay, we assessed how F508del-CFTR membrane density was affected by a number of treatments.

<u>F508del-CFTR: VX-809 incubation</u>

At 37°C, incubation with VX-809 for 24 hours caused a small but significant increase in $\log_{10}\rho$ of F508del-CFTR, (Figure 2a left, see also Supplementary Table I). At 28°C, the magnitude of the increase was greater (Figure 2a right).

<u>F508del-CFTR: R1070W second-site revertant mutation</u>

Introducing the second-site mutation R1070W in the F508del-CFTR background, significantly increased membrane density at 37°C, (Figure 2b left, Supplementary Table I), as well as at 28°C (Figure 2b right, Supplementary Table I). Again, the magnitude of the effect was larger at 28°C.

<u>F508del-CFTR: chronic VX-770 incubation</u>

When comparing cells expressing F508del-CFTR, incubated for 24 hours with VX-809 alone, with those incubated with both VX-809 and VX-770, at 37°C, there was a small but significant decrease in $\log_{10}\rho$ (Figure 2c left, Supplementary Table I). At 28°C the difference was again more pronounced than at 37°C (Figure 2c right).

F508del-CFTR: temperature correction

Because our fluorescence readings are normalized to those obtained from cells expressing WT-CFTR grown on the same 96-well plate, it was not possible to directly compare F508del-CFTR membrane density at the two temperatures. We therefore quantified the difference between the mean $\log_{10}\rho$ of WT-CFTR and F508del-CFTR for each experiment. The $\log_{10}\rho$ values of F508del-CFTR were found to be significantly closer to those of WT-CFTR at 28°C, than at 37°C, (Figure 2d, Supplementary Table I), confirming that the assay can detect temperature correction.

Increasing F508del-CFTR ion channel function

Following addition of extracellular I^- (to reach $[I^-]_{out}$ = 100 mM), CFTR was activated by 10 µM forskolin alone, or by a combination of 10 µM forskolin and 10 µM VX-770 (the latter defined as an acute (a) treatment, as opposed to the 24-hour chronic incubation with VX-770 described above). The normalized YFP fluorescence of HEK293-cells expressing WT-CFTR, F508del-CFTR, or F508del/R1070W-CFTR, after chronic incubation with or without modulators at 37°C or 28°C, was followed over time (Figure 3). The maximal rate of I^- entry was used to summarize CFTR channel function for the different CFTR genotypes, incubation and activation conditions tested (Figure 3e, Supplementary Tables II-III). No significant difference in this metric was detected among the different genotypes/conditions when DMSO (vehicle) was added instead of activators (10 µM forskolin with/without 10 µM VX-770), confirming validity as a negative control.

WT-CFTR

As expected, in cells expressing WT-CFTR, the maximal rate of I^- entry was significantly higher after activation with forskolin, compared to control (DMSO), at both 37°C and 28°C (Figure 3a; Figure 3e WT). However, neither the presence of 10 µM VX-770 in addition to forskolin during activation, nor incubation at 37°C vs 28°C modified quenching rate sufficiently to achieve statistical significance after multiple comparison correction (Figure 3a; Figure 3e, WT, Supplementary Table III).

F508del-CFTR: activation following temperature correction

Even after incubation at 28°C, activation with forskolin alone failed to increase the maximal rate of I^- entry in untreated cells expressing F508del-CFTR (Figure 3b top; Figure 3e F508del bars 1 and 4, Supplementary Table II), reflecting the severe gating defect which persists even after temperature correction. Acute potentiation by VX-770 was required to detect function of the channels reaching the cell surface thanks to temperature-correction: when F508del-CFTR was activated with a combination of forskolin and VX-770, there was a significant increase in the maximal rate of I^- entry compared to control at 28°C but not at 37°C (Figure 3b, bottom; Figure 3e F508del bars 2 and bars 5, Supplementary Table II).

F508del-CFTR: activation following VX-809 correction

In contrast to cells receiving no pharmacological correction at 37°C, the activity of F508del-CFTR channels reaching the cell surface after 24-hour incubation with VX-809 could be detected following acute activation with forskolin and VX-770 (Figure 3b left panel vs 3c left panel; Figure 3e, Supplementary Table II). At 28°C the maximal rate of I^- entry was significantly greater than at 37°C (Figure 3c; Figure 3e, F508del bar 3 vs. bar 6, Supplementary Table III).

F508del-CFTR: rescue of ion channel function by the R1070W mutation

Forskolin activation alone was enough to reveal F508del/R1070W-CFTR channel activity (Figure 3d, Supplementary Table II). The maximal rate of I^- entry was significantly higher at 28°C than at 37°C (Figure 3d; Figure 3e F508del/R1070W, Supplementary Table III).

The rare mutation pIRES2-mCherry-YFPCFTR panel

CF-causing missense CFTR mutations [33-35] were individually introduced in the pIRES2-mCherry-YFPCFTR plasmid, creating a panel of 62 plasmids. WT-CFTR, F508del-CFTR and G551D-CFTR were included for reference.

Following expression of the panel in HEK293 cells, and incubation with no pharmacological correction, probability density distributions for the ρ metric, and plate $\log_{10}\rho$ means were obtained (Supplementary table IV, Supplementary Figure 1). The data is summarized in Figure 4a, which profiles membrane density for each CFTR mutant in the panel. Correlation between our measured ρ and the proportion of CFTR acquiring complex

glycosylation in FRT cells is surprisingly good (r^2=0.65 [33]; r^2=0.48 [34]), considering the differences in expression system and method used (note that correlation between the two published datasets is r^2=0.48).

YFP-CFTR fluorescence quenching experiments were carried out to estimate steady-state CFTR conductance without (DMSO) and with baseline CFTR activation by 10 µM forskolin (Figure 4b-c; Supplementary Table V). Again, results correlate well with published data (r^2=0.68, [33]; r^2=0.60 [34]). Conductance was also measured in the presence of 10 µM forskolin + 10 µM VX770 (Figure 4d). In these conditions, genotypes with high conductance (including WT-CFTR) have faster YFP quenching than can be reliably measured in our system. However, the assay can accurately monitor VX-770 potentiation when CFTR activity is low, as is the case for most mutants. [34]

Relationship between CFTR ion channel function and membrane density

By considering the changes in ion channel function in the context of any changes measured in ρ, our assay allows more accurate inferences on the gating and permeation properties of the CFTR channel molecules active at the cell surface.

Our images are obtained with widefield microscope optics resulting in stray light from out-of-focus planes reaching the photomultiplier. Because of this and of some inaccuracy in automated cell boundary detection, even when virtually no channels are present in the plasma membrane (as happens e.g. for cells expressing F508del-CFTR incubated at 37^0 C) the value of ρ does not fall to zero. To empirically investigate the relationship between G_{CFTR} and ρ, cells expressing F508del-CFTR were treated with increasing concentrations of corrector VX-809, progressively improving both biogenesis/membrane stability and conductance (Figure 5a). Measured G_{CFTR} values as a function of the corresponding ρ values show a roughly linear relationship. The trendline can be extended to cross the ρ axis, extrapolating to an intercept at ρ = 0.23. In addition, extension towards higher membrane densities shows how gating of F508del-CFTR, VX-809-corrected and acutely potentiated by VX-770, reaches levels characteristic of WT-CFTR (without potentiation), consistent with patch-clamp P_O measurements [36].

Data on maximum rate of I^- entry can also be plotted against the corresponding ρ values, measured for the different F508del-CFTR rescue strategies (Figure 5b). A linear interpolation between data points for uncorrected F508del-CFTR and WT-CFTR activated by 10 µM

forskolin describes the ion channel function we would expect from cells with increasing CFTR membrane density, assuming P_O and γ of baseline-activated WT-CFTR. This allows us to infer how rescued F508del-CFTR channels reaching the membrane compare in gating/permeation characteristics to control channels. The resulting x-axis intercept ($\rho = 0.25$) is very similar to that obtained using G_{CFTR} to quantify ion channel function.

Introducing the R1070W revertant mutation in the F508del-CFTR background is shown to be particularly effective in improving gating. Comparing revertant rescue with temperature correction, Figure 5b shows how both strategies similarly increase membrane density but temperature-corrected F508del-CFTR channels at the membrane have very low ion channel function (unless acutely potentiated with VX-770). In contrast, F508del/R1070W channels that reach the membrane have gating and permeation properties equal - or even superior - to WT-CFTR (Figure 5b, cf. F508del/R1070W-CFTR red symbol vs. uncorrected F508del-CFTR blue symbol). Both results are consistent with patch-clamp records indicating a F508del/R1070W-CFTR P_O comparable to that of WT-CFTR, but a much lower P_O for temperature-corrected F508del-CFTR [36, 37] (γ is unaffected by F508del and R1070W mutations [30, 38]).

Plots of G_{CFTR} as a function of ρ for the rare-mutation panel give an overview of processing and gating/permeation defects caused by each missense mutation (Figure 5c). For instance, data points for D579G-CFTR (orange open diamond at coordinates (0.35,41.5)) and F1074L-CFTR (purple (0.42,69.2)), fall close to the WT-CFTR interpolation line, suggesting that channel P_O and γ are not greatly affected by these mutations, and that the low short-circuit currents measured in FRT cells [33, 34] are largely caused by the reduced membrane densities. For G1244E (orange (0.75,7.2)) and S549N (blue (0.83,11)), likely altering the structure of P-loop and signature sequence loops in site 2, respectively, measured ion channel function is much lower than would be expected given the high membrane density. Here low short-circuit currents [33] are likely due to gating defects. Most mutations give reduced membrane densities and a conductance that falls below the interpolation line, suggesting processing defects as well as some degree of impairment in gating/permeation for the molecules that do reach the membrane. We further illustrate the effect of acute treatment with VX-770 for mutations resulting in the strongest potentiation (fold-potentiation >20-fold, Figure 5d). For most of these, but not all, data points for potentiated conductance fall above the interpolation line, suggesting higher P_O and/or greater γ than measured for WT-CFTR in baseline-activated conditions.

Discussion

Many CFTR variants associated with CF, including the most common variant, F508del-CFTR, are characterized by both processing and functional defects. Rescue of either ion channel function or membrane density alone, is not sufficient for effective treatment of patients [14, 16]. Thus therapies combining multiple correctors/potentiators are now seen as most promising [39]. In addition, evidence is emerging that potentiators can negatively interfere with corrector action [27, 28]. All this highlights the potential impact of our assay - capable of discriminating between pharmacological effects due to changes in CFTR membrane localization from those due to altered gating and permeation characteristics – for future CF therapy.

Our results demonstrate that the assay can accurately detect changes in membrane density of CFTR, even when such changes are small and the heterogeneity among cells is large. The effect of VX-809 on F508del-CFTR membrane density at 37°C is small, and often undetectable unless combined with temperature rescue or revertant mutations [26]. Our assay can pick up a minute difference in average membrane density between untreated and VX-809 treated HEK293 cells incubated at 37°C (Figure 2a left). The effect of the second-site revertant mutation R1070W on F508del-CFTR membrane density at 37°C is similarly small when assayed by other groups [26] and by our method (Figure 2b left). In agreement with other studies [27, 28], we observed a small but significant shift in $\log_{10}\rho$ following chronic incubation with VX-770, consistent with the potentiator destabilizing F508del-CFTR at the membrane (Figure 2c left). We were also able to confirm that the membrane density of F508del-CFTR is increased at low temperature [22-24] (Figure 2d). Furthermore, the effect of VX-809 treatment [25], R1070W rescue, and chronic treatment with VX-770 on membrane density is larger when combined with incubation at low temperature (Figure 2 right).

In addition to membrane density, our assay can accurately quantify channel function, using the YFP-CFTR assay. The conditions used here are not optimized to measure high CFTR activities due to measurements hitting the upper limit of the dynamic range of the assay (e.g. for WT-CFTR, Figs. 3 and 4, Supplementary Table III). However, both the "I^- first" protocol [21], measuring the maximal rate of I^- entry ($\frac{\Delta[I^-]_{in}}{\Delta t}$) during CFTR activation, and "I^- last" protocol [31], estimating CFTR conductance by fitting quenching time course after steady-state activation is reached, can accurately quantify the low CFTR activities typically seen in mutants. Both protocols have advantages and disadvantages. While the latter can estimate CFTR conductance more rigorously, unaffected by variability in signal transduction kinetics and

better accounting for changing electrochemical potential gradients, the $\frac{\Delta[I^-]_{in}}{\Delta t}$ readout allows faster data acquisition and less computationally intensive analysis. Our results, confirming results obtained with other techniques (e.g. Ussing chambers, high-throughput electrophysiology), show that both G_{CFTR} ([33, 34]) and $\frac{\Delta[I^-]_{in}}{\Delta t}$ ([15, 40]) provide accurate estimates of CFTR activity.

Accurate quantification of low conductance values is clearly advantageous in characterizing drug response by CFTR mutants, most of which have low residual activity. For instance, our assay detects strong VX-770 potentiation for R347P-, N1303K- and H1085R-CFTR, genotypes giving no significant potentiation over baseline in the Ussing chamber study [34]. While further studies on the functional effects of R347P and H1085R mutations are required, our results on N1303K are consistent with patch-clamp results [41].

Empirical profiling of drug effects on the rare mutation panel can also generate hypotheses on drug mechanism of action. Considering the sites of mutations resulting in the highest VX-770 efficacy (fold-potentiation>20, Figure 5d-f), they appear to link the ATP molecule bound at site 1 to regions close to the narrowest portion of the permeation pathway, thought to constitute the CFTR gate [42, 43], via the two "ball-and-socket" joints [4] interfacing the NBDs to the transmembrane domains (TMDs).

Among these highly VX-770-sensitive mutations, all those surrounding the ATP and NBD/TMD interface introduce charged side chains likely to interact unfavourably with other close charges in the conformation thought closest to the open channel (phosphorylated, ATP-bound human CFTR, 6MSM [44]): the aspartate replacing G1349, in the NBD2 signature sequence, with the γ-phosphate bound at site 1 [45]; the lysine in place of N1303 in the NBD2 "socket", with R1358 in NBD2; the arginine replacing G178, in intracellular loop 1 (ICL1) with K254, E257 and R258 in ICL2; the aspartate replacing H1054, in ICL4, with E543 in the NBD1 X-loop [46]; the arginine in place of H1085, with R1048 in TM10 (for all listed pairs distances between α-carbons are below 10 Å). Because bound ATP at site 1 plays a role in stabilizing the opening transition state and even more the prehydrolytic O_1 state [47], mutations at these sites are likely to slow opening and particularly destabilize the O_1 channel conformation. It is possible that VX-770 binding allows channels to reach an alternative open state, with a different conformation at the interface between site 1 and the TMDs that is particularly stable [31].

The remaining two highly VX-770-sensitive mutations insert prolines, known to restrict backbone flexibility, in a region close to the CFTR gate. The R347P mutation, in TM6, affects a residue important for maintaining a stable conducting pathway [48-50]. The L927P mutation is in the unwound segment of TM8 [51, 52], underlying CFTR's unique channel function [52]. The very low conductance measured after baseline activation in both these mutants, suggests that backbone flexibility at these sites is required for channel opening and/or to maintain a stable conformation with a conducting permeation pathway. VX-770 has been hypothesized to increase conformational flexibility of CFTR [27] overall. It is tempting to speculate that this increased flexibility might particularly concern the extracellular end of CFTR's transmembrane helices, surrounding the CFTR gate.

Acute treatment with VX-770 is seen to be particularly effective on L927P channels, resulting in an ~80-fold potentiation. Patients carrying the L927P mutation are not currently among the genotypes approved for VX-770 treatment (https://pi.vrtx.com/files/uspi_ivacaftor.pdf) [34]. Further investigation is required: patch-clamp recording of how the L927P-CFTR ion channel function is altered by binding of VX-770, and, studies of how native, patient-derived cells respond to chronic, rather than acute, treatment.

But the main advantage of our assay consists in providing simultaneous measurements of ion channel function and membrane density. Currently available high throughput assays report on either CFTR membrane density or CFTR-mediated cellular conductance (G_{CFTR}). G_{CFTR} is the product of 3 factors: the number of channels at the membrane (N), P_O, and γ ($G_{CFTR} = N \cdot P_o \cdot \gamma$). Being able to monitor how compounds (or mutations) affect both number of channels at the membrane and conductance can allow accurate deconvolution of effects on processing (altering N) from those influencing gating and permeation of the channel (affecting P_O and γ, respectively). Obtaining both measurements simultaneously, on the same CFTR-expressing cells, provides a complete description of CFTR molecular characteristics, including accurate information on the gating/permeation characteristics of channels that have reached the membrane. The latter information estimated with our assay is more accurate than can be obtained from separate biochemical and electrophysiological investigations on cultures grown in parallel [33, 34].

Describing each CF-causing mutation with two coordinates (ρ and G_{CFTR}) is a concise, informative way of characterizing mutations (e.g. Figure 5c) and the effects of CFTR

modulators on them (e.g. Figure 5d). Implementing the assay at early stages (compound screening cascades and structure-activity relationship studies) could guide drug development and give valuable insight relevant to patient stratification for clinical trial planning. In addition, given the precedent of the FDA taking laboratory data into account for genotype expansion of the VX-770 label [20], data obtained with high-content in vitro assays could provide licensing authorities with useful material on which to base decisions on regulatory approval for genotypes found only very rarely in the population.

Conclusions

We have developed an assay that rapidly and simultaneously assesses ion channel function and membrane density of different CFTR variants, and their response to compounds. The medium-throughput assay presented here can be usefully exploited to investigate the biophysical and molecular mechanisms underlying CFTR function: initial mutant/compound scans could rapidly identify areas worth further, more detailed investigation using patch-clamp recording and computer simulations. In addition, given the presence of hundreds of rare CF-causing mutations, and the emergence of combination treatments as the most promising therapy for CF, the assay is a powerful tool for better informing the drug development process in CF, hopefully advancing the discovery of effective “precision medicines” providing true curative rather than symptomatic therapy, even to patients carrying rare CFTR mutations.

Methods

Construction of the pIRES2-mCherry-YFPCFTR plasmid

The pIRES2-mCherry-YFPCFTR plasmid was obtained with two sequential subcloning steps. First, a 1.727kb region of pcDNA3.1-YFP-CFTR [21], containing the YFP-coding sequence, was subcloned into pIRES-eGFP-CFTR, a gift from David Gadsby (Rockefeller University), using the NheI and BlpI restriction sites [21]. Subsequently a 0.737 kb region from pIRES2-mCherry-p53 deltaN [53] (Addgene), containing the mCherry-coding segment and part of the IRES, was subcloned into the pIRES-eGFP-YFPCFTR plasmid using the NotI and BmgBI/BtrI restriction sites. This resulted in the pIRES2-mCherry-YFPCFTR plasmid, with the IRES2 positioned between the two open reading frames for mCherry and YFP-CFTR.

HEK293 cell culture and transfection

HEK293 cells were maintained in Dulbecco's modified Eagle's medium (DMEM), supplemented with 2 mM L-glutamine, 100 U/mL penicillin and streptomycin, and 10% fetal bovine serum (all Life Technologies). Cells were seeded in poly-D-lysine-coated, black-walled 96-well plates (Costar, Fisher Scientific), and transiently transfected with the pIRES2-mCherry-YFPCFTR plasmid using Lipofectamine 2000 (Life Technologies). After transfection, cell plates were returned to the 37°C incubator for 24 hours. Prior to imaging plates were incubated for another 24 hours, at 37°C or 28°C, in 100 µL DMEM including DMSO (vehicle), 10 µM VX-809, or 10 µM VX-770 plus 10 µM VX-809 (Selleck Chemicals).

Image acquisition

Before imaging, cells were washed twice with 100 µL standard buffer (140 mM NaCl, 4.7 mM KCl, 1.2 mM MgCl2, 5 mM HEPES, 2.5 mM CaCl2,1mM glucose, pH 7.4). The ImageXpress Micro XLS (Molecular Devices), an automated inverted wide-field fluorescence microscope with a temperature-controlled chamber (set to 37°C or 28°C, as indicated), was used for image acquisition. Protocols for automated fluid additions, enabled by a robotic arm, were created using MetaXpress software (Molecular Devices). For imaging of YFP(H148Q/I152L)-CFTR, a 472 ± 30 nm excitation filter, and a 520 ± 35 nm emission filter were used. Excitation/emission filters at 531 ± 20 nm and 592 ± 20 nm were used for imaging of mCherry.

For localization of CFTR, a 60× objective was used to take 9 16-bit images per well of both fluorophores. To evaluate CFTR function, a 20× objective was used. Two 16-bit images of mCherry were taken, one at the start and one the end of the protocol. In addition, 16-bit images of the YFP fluorescence, were taken at an acquisition frequency of 0.5 Hz. For the I^- first protocol ((A), see below), after 20 s, 50 µL of 300 mM I^- buffer (300 mM NaI, 4.7 mM KCl, 1.2 mM $MgCl_2$, 5 mM HEPES, 2.5 mM $CaCl_2$,1mM glucose, pH 7.4) was added to the standard buffer, so that the final concentration of I^- in the extracellular medium was 100 mM. Another 40 s later, a further 50 µL of a 100 mM I^- buffer containing 40 µM forskolin (100 mM NaI, 4.7 mM KCl, 1.2 mM $MgCl_2$, 5 mM HEPES, 2.5 mM $CaCl_2$,1mM glucose, 40 µM forskolin, pH 7.4) was added, so that the final concentration of forskolin in the extracellular medium was 10 µM, while concentration of I^- and other components remained unaltered. For the I- last protocol ((B), below), after 20 s of imaging, CFTR was activated, in the absence of extracellular iodide, by addition of 50 µl standard buffer containing activating compounds (forskolin or forskolin + VX-770 both to reach final concentrations of 10 µM). After a further 230 s, by which time CFTR is assumed to be gating at steady state [31], 100 mM extracellular iodide (final concentration) was introduced by adding 50 µl of iodide buffer (as standard buffer with 140 mM NaCl replaced with 400 mM NaI). Images were taken for 40 more seconds. Activating compounds were also included in the second addition so as not to alter final extracellular concentrations.

Image analysis

Image analysis was automated using MATLAB mathematical computing software (MathWorks). Separate analysis protocols were implemented to estimate CFTR membrane density and ion channel function.

<u>CFTR membrane density</u>

First, mCherry images were binarized, and basic morphological operations (opening, closing, area opening, and dilation) were carried out to reduce noise. A distance transform with locally imposed minima was used to segment images by means of a watershed transformation and define cell boundaries. Cells were removed from analysis if they had an area of under 108 μm^2 or over 5400 μm^2, if they had a major axis length of less than 32.4 µm, if the area over perimeter was less than 25 or over 300, and if they were touching the edge of the image. A 1.08

µm band, 10 or 5 pixels wide (depending on the resolution of the image), within the border of each cell was defined as the membrane zone.

Background was selected by inverting the binarized and morphologically opened mCherry image, after which it was morphologically closed using a large structuring element to prevent cells from being selected as background. Average background intensity was then subtracted from each pixel, and the YFP and mCherry fluorescence intensity of each cell was normalized to the median YFP and mCherry fluorescence intensities of cells expressing WT-CFTR on the same plate. If the average normalized fluorescence intensity fell below 0 (due to low transfection efficiency and high background noise), cells were removed from analysis.

In order to estimate CFTR membrane density for each cell (defined as ρ, see Results), the average normalized YFP fluorescence intensity within the membrane zone was divided by the average normalized mCherry fluorescence over the entire cell.

$$\rho = \frac{F_{\text{YFP membrane}}}{F_{\text{mCherry cell}}}$$

<u>CFTR ion channel function</u>

For assessment of CFTR function, two different protocols were used. For both, cells were selected based on the mCherry fluorescence image that was taken at the beginning of the protocol.

(A) I^- first Protocol

The baseline fluorescence before addition of I^- was used to normalize YFP fluorescence intensity. The concentration of I^- inside the cells ($[I^-]_{in}$) can be estimated with the following equation [21], in which the binding affinity for I^- (K_I) to YFP(H148Q/I152L) is 1.9 mM [5] and the normalized fluorescence intensity over time (*F(t)*) is determined experimentally.

$$[I^-]_{in} = K_I \frac{(1 - F(t))}{F(t)}$$

Data is collected every 2 seconds, so the change $[I^-]_{in}$ observed at each time point can be estimated and used to calculate the rate of I^- entry (in mM/s):

$$\frac{\Delta[I^-]_{in}}{\Delta t} = \frac{[I^-]_{in}(t) - [I^-]_{in}(t-1)}{2\ \text{s}}$$

The maximal observed rate of I^- entry is used as a measure of cellular anion conductance. To determine whether there was increased CFTR-mediated anion conductance, the maximal rate of I^- entry after addition of forskolin (which activates CFTR by cAMP dependent

phosphorylation), was compared to the maximal rate of I^- entry after addition of DMSO (vehicle, negative control).

(B) I^- last Protocol

CFTR activation (by addition of 10 μM forskolin with or without 10 μM VX-770, as indicated) was allowed to reach steady state in the absence of I^- and quenching of YFP in the 40 s following extracellular I^- addition was measured. A simple mathematical model was used to fit observed fluorescence quenching, and estimate CFTR conductance as described [31]. Briefly, the model includes four free parameters: CFTR conductance at steady-state (G_{CFTR}), membrane potential at steady-state, immediately prior to I^- addition (V_M), and conductance (G_{trans}) and time constant (τ_{trans}) of a transient, endogenous non-CFTR anion conductance. The values of the four parameters were estimated by minimizing the sum of squared residuals obtained by comparing the time course of the observed average fluorescence intensity within cells to the proportion of anion-free YFP chromophore predicted by the model (both normalized to the time before I^- addition). However, when the quenching time course was too fast and did not provide enough information to uniquely identify all four parameters, the value of the latter two parameters was constrained to the average values obtained with negative controls, and only G_{CFTR} and V_M were estimated [31].

For both protocol (A) and (B) the value obtained from analysis of the observed YFP-CFTR fluorescence quenching ($\frac{\Delta[I^-]_{in}}{\Delta t}$ and G_{CFTR}, respectively) was corrected for variations in transfection efficiency, using the mean $F_{mCherry}$ within the cell selection normalized to $F_{mCherry}$ measured for WT in the same plate.

Statistical analysis

Because ρ values approach a log-normal distribution, values were log transformed before performing statistical analysis, allowing parametric testing of the data. To determine whether the observed differences in ρ, $\frac{\Delta[I^-]_{in}}{\Delta t}$, or G_{CFTR} resulting from experimental manipulation and/or mutations were statistically significant, we performed either paired t-tests, pairing conditions tested on the same plate, or independent t-tests. When required, either a Bonferroni or a Benjamini-Hochberg correction was applied to adjust for multiple comparisons. Data in graphs represent mean ± SEM, and the significance level was pre-specified as $\alpha = 0.05$. Statistical analysis was carried out using MATLAB (MathWorks), SigmaPlot (Systat Software), SPSS (IBM), or Excel (Microsoft).

Author Contributions

Experiments were conceived and designed by SP, EL and PV, after discussion with LDG and CH. SP and EL, with the help of ACS, CH and EH carried out the molecular biology, ran the fluorescence assay acquisition and ran image analysis. SP, with the help of CH, implemented the image analysis protocols and the mathematical model in the MATLAB environment. Manuscript was written by SP, EL and PV. All authors read and commented on the final draft of the manuscript.

Acknowledgements

EL was supported by grant 15UCL04, funded by the Sparks charity and Cystic Fibrosis Trust. SP was supported by grant SRC005 funded by the Cystic Fibrosis Trust. CH was supported by EPSRC grant EP/F500351/1. We thank Dr William Andrews, Central Molecular Laboratory, UCL for help with molecular biology.

Conflict of interest declaration

The authors declare no conflicts of interest.

References

1. Elborn, J.S. *The Lancet*. **388**, 2519-2531 (2016).

2. Rommens, J.M., et al. *Science*. **245**, 1059-1065 (1989).

3. Riordan, J.R., et al. *Science*. **245**, 1066-73 (1989).

4. Csanády, L., P. Vergani, and D.C. Gadsby. *Physiol Rev.* **99**, 707-738 (2019).

5. Galietta, L.J.V., P.M. Haggie, and A.S. Verkman. *FEBS Lett.* **499**, 220-224 (2001).

6. Galietta, L.V.J., S. Jayaraman, and A.S. Verkman. *Am J Physiol Cell Physiol.* **281**, C1734-C1742 (2001).

7. Pedemonte, N., et al. *Mol Pharmacol*. **67**, 1797-1807 (2005).

8. Pedemonte, N., et al. *J. Clin. Invest.* **115**, 2564-2571 (2005).

9. Yang, H., et al. *J. Biol. Chem.* **278**, 35079-35085 (2003).

10. Ma, T., et al. *J. Biol. Chem.* **277**, 37235-37241 (2002).

11. Van Goor, F., et al. *Proc Natl Acad Sci USA*. **106**, 18825-18830 (2009).

12. Van Goor, F., et al. *Am J Physiol Lung Cell Mol Physiol*. **290**, L1117-1130 (2006).

13. Gentzsch, M. and M.A. Mall. *Chest*. **154**, 383-393 (2018).

14. Flume, P.A., et al. *Chest*. **142**, 718-724 (2012).

15. Van Goor, F., et al. *Proc Natl Acad Sci USA*. **108**, 18843-18848 (2011).

16. Clancy, J.P., et al. *Thorax*. **67**, 12-18 (2012).

17. Wainwright, C.E., et al. *N. Engl. J. Med.* **373**, 220-231 (2015).

18. Davies, J.C., et al. *N Engl J Med*. **379**, 1599-1611 (2018).

19. Keating, D., et al. *New England Journal of Medicine*. **379**, 1612-1620 (2018).

20. Ratner, M. *Nature Biotechnology*. **35**, 606 (2017).

21. Langron, E., et al. *Br J Pharmacol*. **174**, 525-539 (2017).

22. Denning, G.M., et al. *Nature*. **358**, 761-764 (1992).

23. Rennolds, J., et al. *Biochem Biophys Res Commun.* **366**, 1025-1029 (2008).

24. Wang, X., et al. *Traffic*. **9**, 1878-1893 (2008).

25. He, L., et al. *FASEB J.* **27**, 536-545 (2013).

26. Okiyoneda, T., et al. *Nat Chem Biol*. **9**, 444-454 (2013).

27. Cholon, D.M., et al. *Sci Transl Med*. **6**, 246ra96 (2014).

28. Veit, G., et al. *Sci Transl Med*. **6**, 246ra97 (2014).

29. Farinha, Carlos M., et al. *Chem Biol.* **20**, 943-955 (2013).

30. Thibodeau, P.H., et al. *J Biol Chem*. **285**, 35825-35835 (2010).

31. Langron, E., S. Prins, and P. Vergani. *Br J Pharmacol*. **175**, 3990-4002 (2018).

32. Shaner, N.C., et al. *Nat Biotechnol*. . **22**, 1567 (2004).

33. Sosnay, P.R., et al. *Nat Genet*. **45**, 1160-1167 (2013).

34. Van Goor, F., et al. *J Cyst Fibros*. **13**, 29-36 (2014).

35. Yu, H., et al. *J Cyst Fibros*. **11**, 237-245 (2012).

36. Wang, Y., et al. *American Journal of Physiology-Lung Cellular and Molecular Physiology*. **315**, L846-L857 (2018).

37. Liu, J., et al. *Br J Pharmacol*. **175**, 1017-1038 (2018).

38. Dalemans, W., et al. *Nature*. **354**, 526-528 (1991).

39. Holguin, F. *N. Engl. J. Med.* **379**, 1671-1672 (2018).

40. Billet, A., et al. *Front Pharmacol.* **8** (2017).

41. DeStefano, S., M. Gees, and T.-C. Hwang. *Journal of Cystic Fibrosis* (2018).

42. El Hiani, Y. and P. Linsdell. *J Biol Chem*. **285**, 32126-32140 (2010).

43. Gao, X. and T.-C. Hwang. *Proc Natl Acad Sci USA*. **112**, 2461-2466 (2015).

44. Zhang, Z., F. Liu, and J. Chen. *Proc Natl Acad Sci USA* (2018).

45. Bompadre, S.G., et al. *J. Gen. Physiol.* **129**, 285-298 (2007).

46. He, L., et al. *J. Biol. Chem.* **283**, 26383-26390 (2008).

47. Sorum, B., B. Töröcsik, and L. Csanády. *eLife*. **6**, e29013 (2017).

48. Cotten, J.F. and M.J. Welsh. *J. Biol. Chem.* **274**, 5429-5435 (1999).

49. Kopeikin, Z., et al. *J Gen Physiol*. **136**, 659 (2010).

50. Cui, G., et al. *J Biol Chem*. **288**, 20758-20767 (2013).

51. Corradi, V., et al. *Biophys J*. **114**, 1751-1754 (2018).

52. Liu, F., et al. *Cell*. **169**, 85-95.e8 (2017).

53. Lin, S.-C., E.D. Karoly, and D.J. Taatjes. *Aging Cell*. **12**, 863-872 (2013).

Figures and figure legends

Figure 1

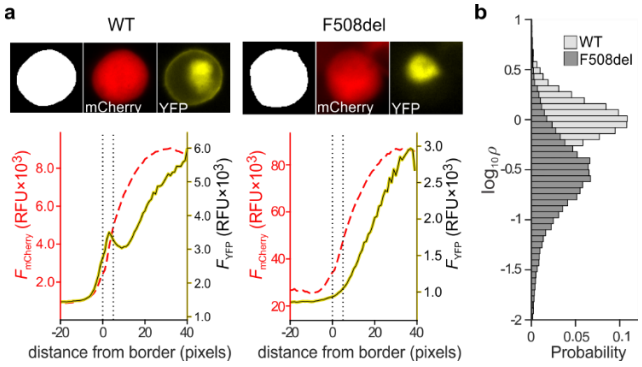

(**a**) Image analysis of individual representative HEK293 cells transfected with pIRES2-mCherry-YFP-WT-CFTR (left), and pIRES2-mCherry-YFP-F508del-CFTR (right). Upper panels: boundary delimiting cell (white) from non-cell (black) is obtained from mCherry image (centre). CFTR cellular localization is obtained from YFP image (right). Lower panels: average mCherry fluorescence intensity (F_{mCherry}, red dashed line), and average YFP fluorescence intensity (F_{YFP}, solid yellow line), as a function of the distance from cell border. Membrane density is defined as

$$\rho = \frac{F_{\mathrm{YFP\ membrane}}}{F_{\mathrm{mCherry\ cell}}}$$

where $F_{\mathrm{YFP\ membrane}}$ is the average fluorescence intensity within the 'membrane' zone, set between 0 and 5 pixels from the cell border. (**b**) Probability density distribution of $\log_{10}\rho$ for cells expressing YFP-WT-CFTR (light grey), and YFP-F508del-CFTR (dark grey), incubated at 37 °C. For the WT cell shown, ρ=1.60; for the F508del cell, ρ=0.25.

Figure 2

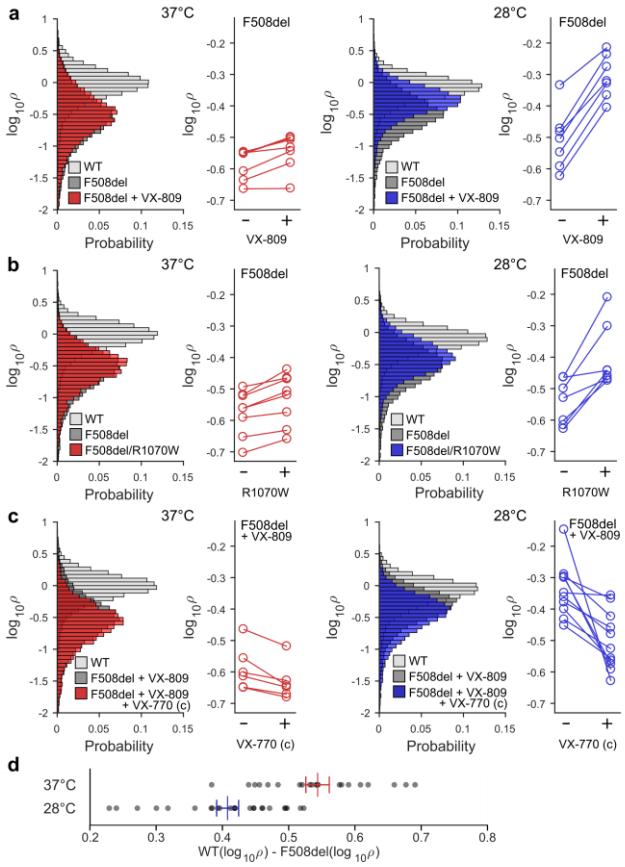

CFTR Membrane density ($\log_{10}\rho$) in HEK293 cells expressing WT-CFTR, F508del-CFTR, or F508del/R1070W-CFTR. Effects of chronic treatment with 10 µM VX-809 (**a**), R1070W rescue (**b**), and chronic treatment with 10 µM VX-809 + 10 µM VX-770 (**c**), on $\log_{10}\rho$ at 37°C (left, red) and 28°C (right, blue). Conditions of final incubation were maintained during image acquisition. The probability distributions in the panels on the left, contain $\log_{10}\rho$ measurements from thousands of cells, pooled from all experiments. For statistical analysis, mean $\log_{10}\rho$ values determined in independent experiments, and paired per plate, were used (displayed in panels on the right) (**d**) Before imaging, plates were incubated at 37°C, or 28°C for 24 hours. For each plate, the difference between mean $\log_{10}\rho$ for WT-CFTR and F508del-CFTR was calculated (WT($\log_{10}\rho$) - F508del($\log_{10}\rho$), grey dots). Red (37°C) and blue (28°C) lines show mean ± SEM, calculated from 21(37°C) and 25(28°C) within-plate difference estimates.

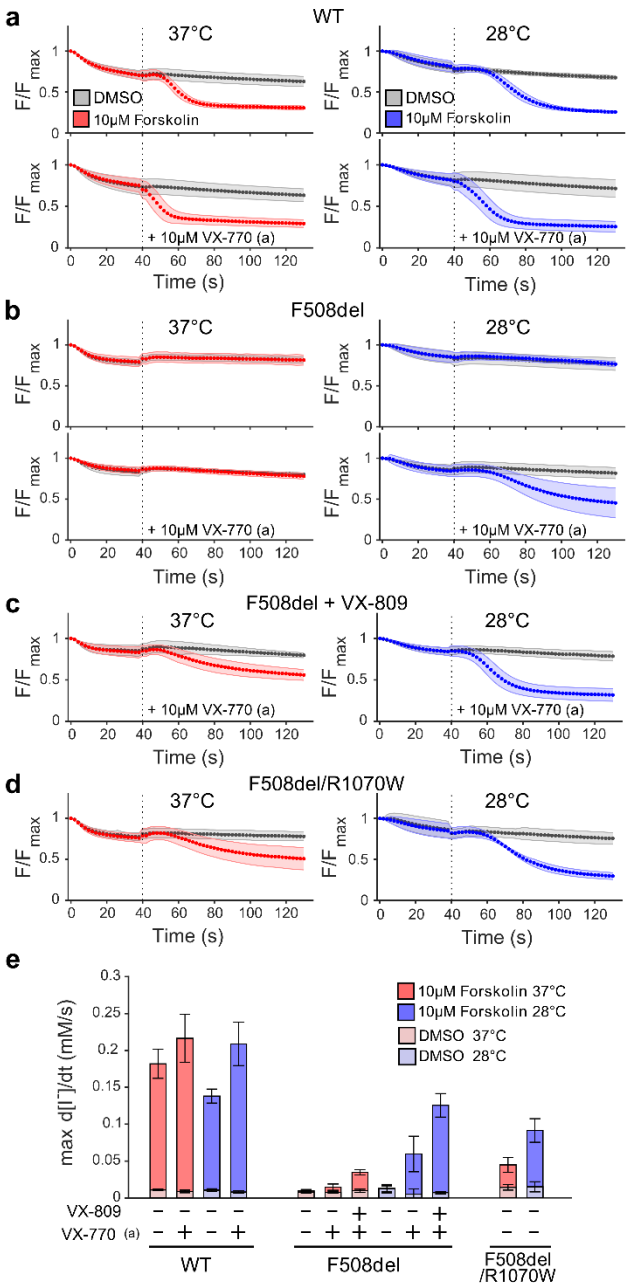

Figure 3

(**a-d**) Quenching of YFP fluorescence in HEK293 cells expressing WT-CFTR (**a**), F508del-CFTR treated with DMSO (**b**) or with VX-809 (**c**), and R1070W/F508del-CFTR (**d**). Prior to imaging plates were incubated for 24 hours, at 37°C (left panels, red) or 28°C (right panels, blue). This final incubation temperature was maintained throughout image acquisition. At time point 0 s I^- was added to the extracellular medium. At 40 s forskolin and, where indicated, VX-770 (acute, a) was added (dotted line), both to a final concentration of 10 μM. The baseline fluorescence before addition of I^- (F_{max}), was used to normalize YFP fluorescence intensity. (**e**) The maximal rate of I^- entry (d[I^-]/dt_norm) is used to summarize CFTR function for genotypes and conditions shown in (**a-d**).

Figure 4

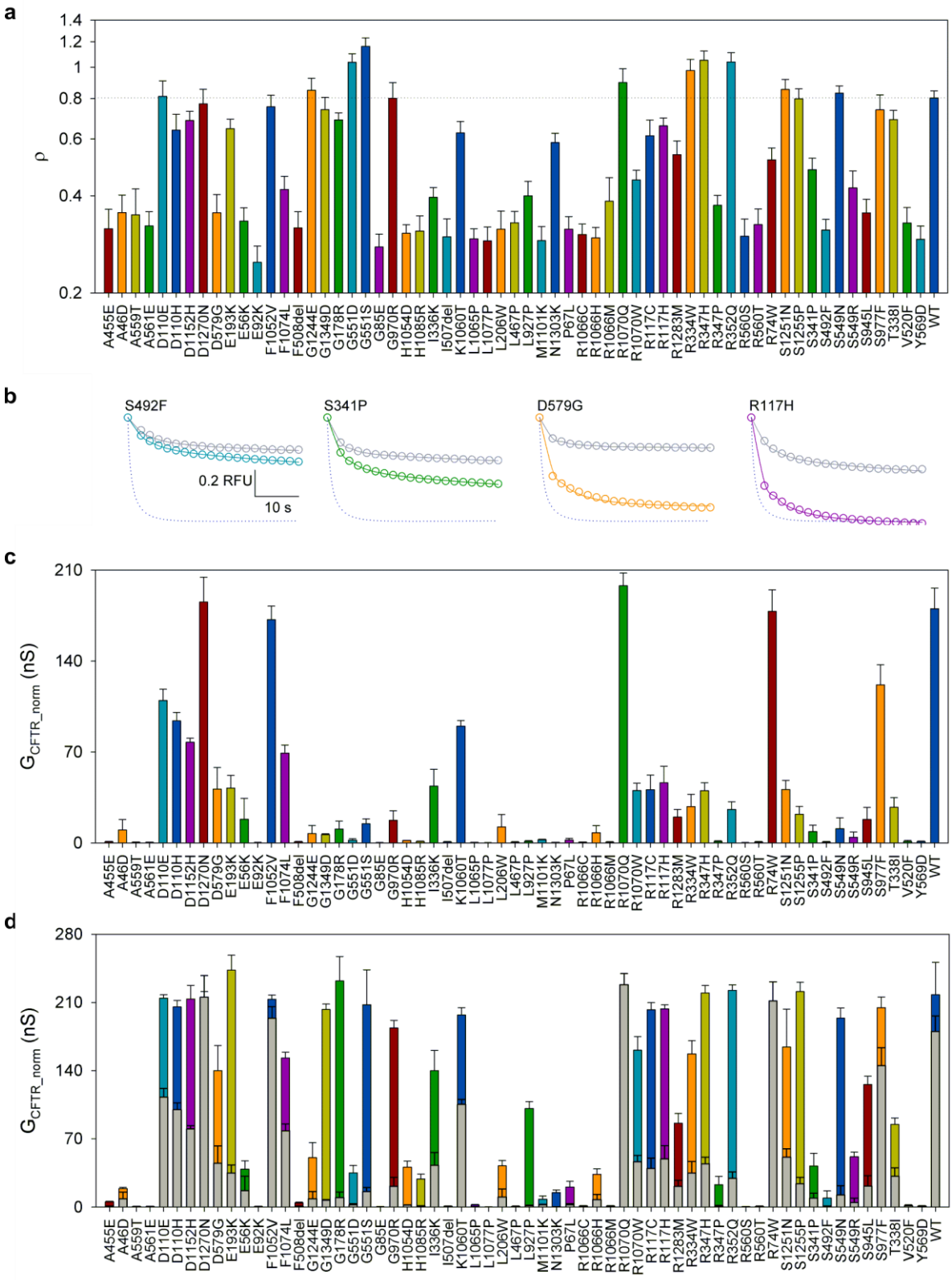

Rare mutation profiling. (**a**) Mean ρ (n ≥ 9) of all mutations in the panel. Dotted line indicates mean ρ for WT-CFTR. For ρ distributions, mean ρ and n values for each mutant see Supplementary Information Figure1 and Supplementary Table IV. (**b**) Observed YFP

quenching time course in the presence of DMSO (grey circles) or 10 μM forskolin (coloured circles) for selected mutations. Solid lines show predicted change in proportion of anion-free YFP. For S492F-, S341P-, D579G and R117H-CFTR estimated parameters were G_{CFTR}: 1.6 nS, 2.1 nS, 57.7 nS, 46.5 nS; V_M: -69 mV, -40 mV, -74 mV, -50 mV; 14.8 nS $\leq G_{trans} \leq$ 19.9 nS; 4.7 s $\leq \tau_{trans} \leq$ 6.8 s. WT-CFTR quenching in 10 μM forskolin (dark blue dotted line) shown for comparison. (**c**) Normalized CFTR conductance of rare mutation panel after activation with 10 μM forskolin. n $\geq$ 3. For G_{CFTR_norm} and n values for each mutant see Supplementary Information S3. (**d**) Potentiation of rare mutation panel by VX-770. Grey bars show values following activation with 10 μM forskolin alone, coloured bars with further addition of acute 10 μM VX-770.

Figure 5

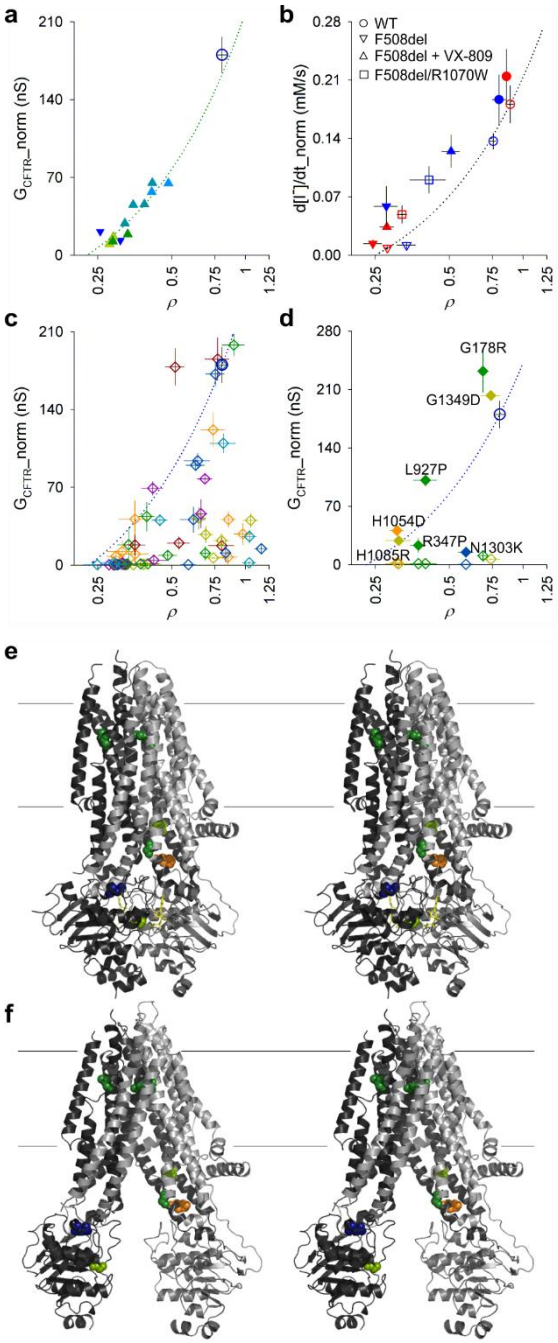

Investigating permeation/gating characteristics. (**a**) Relationship between normalized CFTR conductance and membrane density in cells expressing F508del-CFTR with no correction (blue ∇) or incubated with increasing concentrations of VX-809 (1 nM to 10 μM, green to light blue Δ), all after activation with 10 μM forskolin and acute potentiation with 10 μM VX-770. F508del-CFTR incubation and measurements were at 28°C. Green dotted line shows linear regression using only F508del-CFTR data points on graph (slope = 281.7, constant = -63.7, resulting in an x-axis intercept at ρ = 0.23). Mean value for WT-CFTR activated with 10 μM forskolin alone is shown for reference (from (**c**), large dark blue empty circle). (**b**) Relationship

between maximal rate of I^- influx and ρ in HEK293 cells expressing WT-CFTR, F508del-CFTR, and F508del/R1070W-CFTR, at 37°C (red) and 28°C (blue). 10 μM forskolin was used to activate CFTR. Empty symbols indicate activation with forskolin alone. Solid symbols indicate further acute potentiation with 10 μM VX-770. Dotted line: linear interpolation between data obtained at 37°C for uncorrected F508del-CFTR and WT-CFTR, both without acute VX-770 potentiation; slope = 0.284, constant = -0.071, resulting in an x-axis intercept at ρ = 0.25. (**c**) Relationship between baseline G_{CFTR_norm} (10 μM forskolin) and ρ for rare mutation panel. Colours as in Figure 4. WT-CFTR is highlighted as a large, dark blue, empty circle. The dark blue dotted line (slope = 314.1, constant= -72.3) shows linear interpolation between WT data points and x-axis intercept set at ρ=0.23, as obtained in (**a**). (**d**) Mutants with largest fold potentiation by VX-770 (ratio between conductance obtained in 10 μM forskolin + 10 μM VX-770 over that in 10 μM forskolin alone > 20-fold). Empty diamonds indicate baseline activation with 10 μM forskolin alone, solid diamonds indicate activation following acute potentiation with 10 μM forskolin + 10 μM VX-770. (**e**) Cartoon representation (cross-eye stereo) of phosphorylated, ATP-bound human CFTR (6msm [44]) highlighting positions of mutations with most efficacious VX-770 potentiation. Mutated residues are shown as spheres, colour-coded as in (**d**). Fine horizontal lines show approximate position of membrane boundary. (**f**) As in (**e**) but using atom coordinates of dephosphorylated human CFTR (5uak [52]).